Improved description of the shape parameter in modeled cloud-top droplet size distributions

Lianet H. Pardo[1], Luiz A. T. Machado[1], Micael A. Cecchini[2], Eder Vendrasco[1], Thiago Biscaro[1], and Jean-François Ribaud[1]

[1]Centro de Previsão de Tempo e Estudos Climáticos, Instituto Nacional de Pesquisas Espaciais, Cachoeira Paulista, Brasil
[2]Departamento de Ciências Atmosféricas, Instituto de Astronomia, Geofísica e Ciências Atmosféricas, Universidade de São Paulo, Brasil

Correspondence to: Lianet H. Pardo (lianet.pardo@cptec.inpe.br)

Abstract. This research explores the influence of the level of detail used for describing the droplet size distributions (DSD) in modeled clouds, comparing with observations. A bin microphysics parameterization is used as a benchmark to propose an adjustment in the shape parameter of the DSD, for an improved description of hidrometeors and their interactions in bulk microphysics models. The modeled DSD evolution during a warm cloud development is compared to the results obtained from HALO airplane measurements during the ACRIDICON-CHUVA campaign in the Amazon dry-to-wet season transition. The comparison shows an agreement between the observed and simulated trajectories in the Gamma phase space, providing a suitable representation of the DSD evolution. Two different bulk microphysics parameterizations were evaluated regarding the evolution of the DSD and using the bin scheme as a reference. The results show the weakness of bulk schemes in representing trajectories in the Gamma phase space; thus, a new closure is proposed for better comparisons to the reference. The new closure resulted in an improvement of the representation of the DSD evolution, cloud droplet effective diameter and rain mixing ratio in a warm phase, single column simulation. In a cloud resolving simulation of a convective real case, the proposed closure caused notable modifications in the structure of the clouds, through changes in the droplet to ice conversion rates, sedimentation and vertical velocity.

1 Introduction

Cloud microphysics parameterizations have strongly evolved, and new sets of schemes have been proposed over the past years (Khain et al., 2004; Gilmore et al., 2004; Khain et al., 2010; Mansell et al., 2010; Lim and Hong, 2010; Loftus et al., 2014; Thompson and Eidhammer, 2014). However, due to the complexities of the physical processes in determining the evolution of hydrometeor size distributions during the cloud life cycle, large uncertainties remain in all types of schemes. The lack of knowledge about the characteristics of the effects of atmospheric aerosols on clouds and precipitation is an important source of uncertainty in parameterizations, as are the descriptions of ice and mixed phase processes and the effects of turbulence and entrainment (Khain et al., 2015).

Although bin schemes are more accurate and flexible (Berry and Reinhardt, 1974; Enukashvily, 1980; Tzivion et al., 1987), their high computational cost makes them less useful for operational applications or for research activities that do not focus on the effects of microphysics processes. For most of those applications, bulk schemes are more frequently employed (Lin et al., 1983; Ferrier, 1994; Thompson et al., 2008; Morrison et al., 2009). However, the assumption of a predefined function for hydrometeor size distributions limits the range of situations that can be simulated with a reasonable degree of accuracy.

In bulk microphysics parameterizations, the gamma function (Eq. 1) is one of the more common ways to represent the droplet size distributions (DSDs), it includes as a particular case the exponential function ($\mu = 0$), which is also frequently employed to this effect (Khain et al., 2015):

$$N(D) = N_0 D^{\mu} exp(-\Lambda D) \tag{1}$$

where N_0 (cm$^{-3}\mu$m$^{-1-\mu}$), μ (dimensionless) and Λ (μm^{-1}) are the intercept, shape and curvature parameters, respectively, and $N(D)$ is the number of droplets with diameter D per cm^3 of air.

To solve for the three parameters of the gamma function, three moments would be necessary. However, most bulk microphysical parameterizations – single- or double-moment schemes – do not predict enough moments of the DSD to properly describe their variability. As a closure, the μ parameter of the gamma DSD is commonly fixed or evaluated (Grabowski, 1998; Rotstayn and Liu, 2003; Morrison and Grabowski, 2007). Due to its functional relationship, the choice of μ determines the values of N_0 and Λ. Nevertheless, choosing the value or the expression used to evaluate μ is complicated because of the range of possible values that were reported in the literature (Miles et al., 2000). Switching between different methods for μ can lead to a 25% increase in cloud water path (Morrison and Grabowski, 2007) and a 50% variation in the condensation rate (Igel and van den Heever, 2017). Although triple-moments schemes already allow to determine the three parameters of the gamma function without additional considerations (Milbrandt and Yau, 2005a, b; Szyrmer et al., 2005), they are still too computationally costly for many applications of practical interest, such as operational forecasts or even research activities. Thus, the description of hydrometeor size distributions in bulk parameterizations continues to be one of the major questions for the microphysics modeling community.

The main goal of this study is to analyze the influence of the level of complexity employed in the description of the DSD in models. The DSD evolution during the growth stage of a warm cloud, as simulated by different microphysics parameterizations, is compared with in-cloud measurement data provided by Cecchini et al. (2017b). According to the insights obtained from the bin simulations, a new approach to parameterize the μ parameter in bulk schemes is proposed and tested.

2 Modeling approach

2.1 Kinematic Driver

Warm microphysical processes were simulated using a bin parameterization (Tzivion et al., 1987; Feingold et al., 1988; Tzivion et al., 1989) inside a single-column model (Shipway and Hill, 2012), where the vertical velocity is prescribed.

The prognostic variables of the Kinamtic Driver (KiD) are potential temperature (K) and water vapor, hydrometeor and aerosol mixing ratios (kg kg^{-1}). It uses the Exner pressure as a fixed vertical coordinate and the total variance-diminishing scheme (Leonard et al., 1993) as the default advection scheme. Its prognostic variables are held on "full" model levels, while the vertical velocity and density are held on both “full” and “half” levels such that the grid can be used as a Lorenz-type (Lorenz, 1960) or Charney-Phillips-type (Charney and Phillips, 1953) grid.

The KiD model was conceived as a kinematic framework to compare different microphysics parameterizations without addressing the microphysics-dynamics feedbacks. Thus, obtaining precise quantitative simulations with KiD cannot be expected; nevertheless, it can provide important qualitative information about the behavior of hydrometeors during the life cycle of clouds.

In our simulations, a 1 s time step was used for both dynamics and microphysics algorithms during an integration time of 1200 s (20 min). For the vertical domain, a 120-level grid was defined with a 50-m grid spacing from 0 m to 6000 m of altitude.

As initial conditions, vertical profiles of potential temperature and water vapor mixing ratio from an in situ atmospheric sounding[1] were provided (Fig. 1a). We used the 12Z sounding, on September 11, 2014, from Boa Vista-RR, Brazil, for coherence with the atmospheric conditions where the data of the AC09 flight were collected, intending to use those measurements for comparisons here. This flight was performed by the High Altitude and Long Range Research Aircraft (HALO) on the same date of the aforementioned sounding (local dry-to-wet season transition), as part of the ACRIDICON-CHUVA campaign (Wendisch et al., 2016; Machado et al., 2014). It sampled the top of growing convective cumulus, starting close to the local noon, over remote regions of the Amazon, where there is relatively homogeneous conditions, due to the characteristics of the surface, and low aerosol concentrations. The potential temperature and water vapor profiles from the sounding resembled the data measured by the AC09 flight, but with a greater resolution and vertical domain, thus making them more convenient to define the model initial conditions. The sounding data were interpolated to match the model resolution and then smoothed to represent a more general situation.

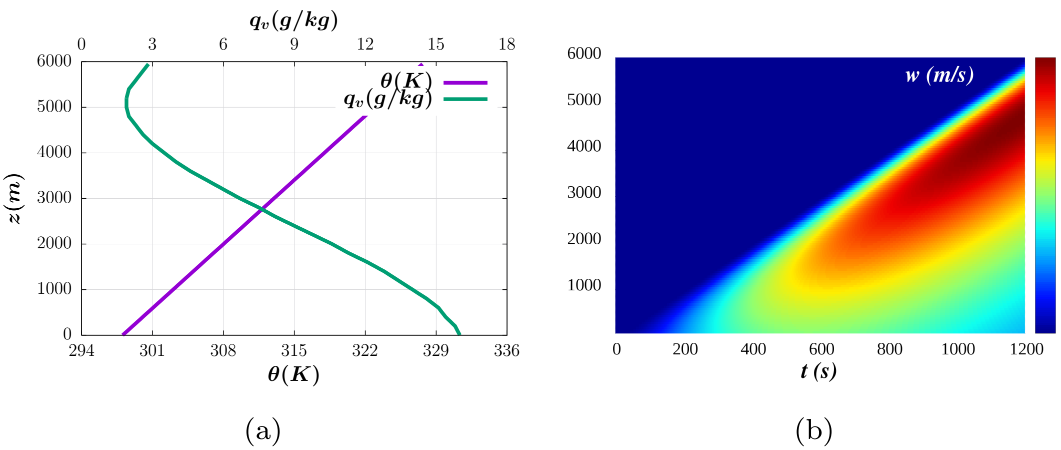

Figure 1. Model configuration: (a) initial conditions and (b) prescribed field of vertical velocity

[1]http://weather.uwyo.edu/upperair/sounding.html

Here, the vertical velocity field ($w(z,t)$) was constructed based on the idea of having a layer of positive buoyancy, where a parcel updraft velocity would increase with height until reaching the negative buoyancy layer. The defined time dependence for the velocity maximum and its height roughly simulate the acceleration that the air must experience and the progressive destabilization of the air column (Fig. 1b).

$$w(z,t) = \begin{cases} W \sin\left(\frac{\pi}{2}\frac{t}{T}\right) e^{-\frac{1}{2}\log^2(0.004t - 0.0008z)} & (0.2z - t) < 0 \\ 0 & otherwise \end{cases} \tag{2}$$

In Eq. 2, W represents the maximum updraft speed (with respect to both height and time) in m s^{-1} and T is the length of the simulation in s. The value of W was set to 5 m s^{-1} taking into account the measurements of the ACRIDICON-CHUVA AC09 flight, where the vertical velocity oscillated between 0 m s^{-1} and 8 m s^{-1} (Cecchini et al., 2017a).

2.2 Weather Research and Forecasting Model

2.3 Microphysics representation

For the most realistic simulations performed in this work, we have used the TAU[2] size-bin-resolved microphysics scheme that was first developed by Tzivion et al. (1987, 1989) and Feingold et al. (1988) with later applications and development documented in Stevens et al. (1996); Reisin et al. (1998); Yin et al. (2000a, b) and Rotach and Zardi (2007).

TAU differs from other bin microphysical codes because it solves for two moments of the drop size distribution in each of the bins rather than solving the equations for the explicit size distribution at each mass/size point, which allows for a more accurate transfer of mass between bins and alleviates anomalous drop growth.

In this version of the TAU microphysics[3], the cloud drop size distribution is divided into 34 mass-doubling bins with radii ranging between 1.56 μm and 3200 μm. The method of moments (Tzivion et al., 1987) is used to compute mass and number concentrations in each size bin resulting from diffusional growth (Tzivion et al., 1989), collision-coalescence and collisional breakup (Tzivion et al., 1987; Feingold et al., 1988). Sedimentation is performed with a first-order upwind scheme. Aerosols are represented by a single prognostic variable, its bulk number concentration, that was initialized as 800cm^{-3}. It is assumed to have a log-normal distribution, with a median radius of 0.05μm and a geometric standard deviation of 1.5. The hygroscopicity of the aerosols was considered as 0.1, according to previous characterizations of the aerosol over the Amazon (Gunthe et al., 2009; Martin et al., 2010; Pöhlker et al., 2016).

In addition, two bulk microphysics parameterizations were used to evaluate and analyze its performance: the schemes described by Thompson et al. (2008) and Morrison et al. (2009).

The parameterization of Thompson et al. (2008) is a single-moment scheme with respect to the warm phase variables, where cloud droplets are assumed to follow a gamma distribution. This scheme is based on Thompson et al. (2004), and it includes several improvements to various physical assumptions in an attempt to equate a full double-moment (or higher order) scheme. One of them is the introduction of an expression for the gamma distribution shape parameter for cloud water droplets (μ) based

[2]The acronym TAU refers to the Tel Aviv University, where it was primarily developed

[3]Version available at https://www.esrl.noaa.gov/csd/staff/graham.feingold/code/ (Accessed on: 04/11/2017)

on observations, which is specifically addressed in this work (Eq. 3).

$$\mu = \frac{1000}{N_d} + 2 \tag{3}$$

In Eq. 3, N_d represents the droplet concentration (cm^{-3}), which has a fixed value (as in every single-moment parametrization), and should be defined by the users according to the mean conditions of the simulated case. In this scheme, an upper bound of 15 on the value of μ was defined.

The scheme of Morrison et al. (2009) predicts the mass mixing ratio and number concentration of hydrometeors, i.e., a double-moment scheme. Cloud droplets are also represented by a gamma distribution, where the μ parameter is a function of the predicted droplet number concentration, following the observations of Martin et al. (1994) (Eq. 4, with minimum and maximum values of 2 and 10, respectively).

$$\mu = (5.714 \times 10^{-4} N_d + 0.2714)^{-2} - 1. \tag{4}$$

Both schemes use the following expressions to calculate Λ and N_0:

$$\Lambda = \left(\frac{\frac{\pi}{6} \rho_w N_d \Gamma(\mu+4)}{r_c \Gamma(\mu+1)} \right)^{\frac{1}{3}} \tag{5}$$

$$N_0 = \frac{N_d \Lambda^{\mu+1}}{\Gamma(\mu+1)} \tag{6}$$

where ρ_w represents the liquid water density (g m^{-3}) and r_c is the cloud liquid water content (g m^{-3}).

2.4 Phase spaces

If we consider a system consisting of a population of drops that follows a Gamma size distribution, then it is possible to track its evolution in the phase space determined by the three Gamma parameters (N_0, μ and Λ). The "Gamma phase space" representation of the AC09 flight (RA1 in Cecchini et al. (2017b)) was taken as a reference to evaluate the performance of the microphysics parameterizations here. Cecchini et al. (2017b) obtained this information by fitting a Gamma function to the DSD data measured by an airborne cloud droplet probe (Lance et al., 2010; Molleker et al., 2014) at the tops of growing convective clouds.

The Thompson et al. (2008) and Morrison et al. (2009) bulk schemes determine the Gamma parameters in every time step; thus, its simulations can be directly represented in the Gamma phase space. However, for taking the simulations of the TAU scheme as a reference with respect to those schemes and compare it with the results of Cecchini et al. (2017b), a Gamma function must be fitted from its explicit size distribution. For coherence with the results of Cecchini et al. (2017b), we conserved the zeroth (M_0), second (M_2) and third (M_3) moments of the bin DSDs to obtain the three Gamma parameters (Equations 8, 9 and 6, where $N_d \equiv M_0$). We restricted our analysis to drops with diameters smaller than 50 μm to avoid rain drops, also for coherence with the analysis of Cecchini et al. (2017b), although there is no significant quantity of drops in this size interval, at the simulated cloud-top.

$$G = \frac{M_2^3}{M_3^2 M_0} \tag{7}$$

$$\mu = \frac{6G - 3 + \sqrt{1+8G}}{2(1-G)} \tag{8}$$

$$\Lambda = \frac{(\mu+3)M_2}{M_3} \tag{9}$$

3 Results

3.1 Observation vs simulation

Figure 2 shows N_d, D_{eff} and the mixing ratio of cloud droplets (q_c), for the entire simulation. Note that the upward advection causes a maximum of N_d at cloud-top for all times. As droplets ascend and mix with new droplets, they grow by diffusion of vapor and collision-coalescence. As a consequence, D_{eff} and q_c are larger in upper levels at the last times of the simulation. The cloud-top was defined as the last model level, from surface to top, where the droplets concentration was larger than 100 per cm^3. It is represented by black lines in Fig. 2.

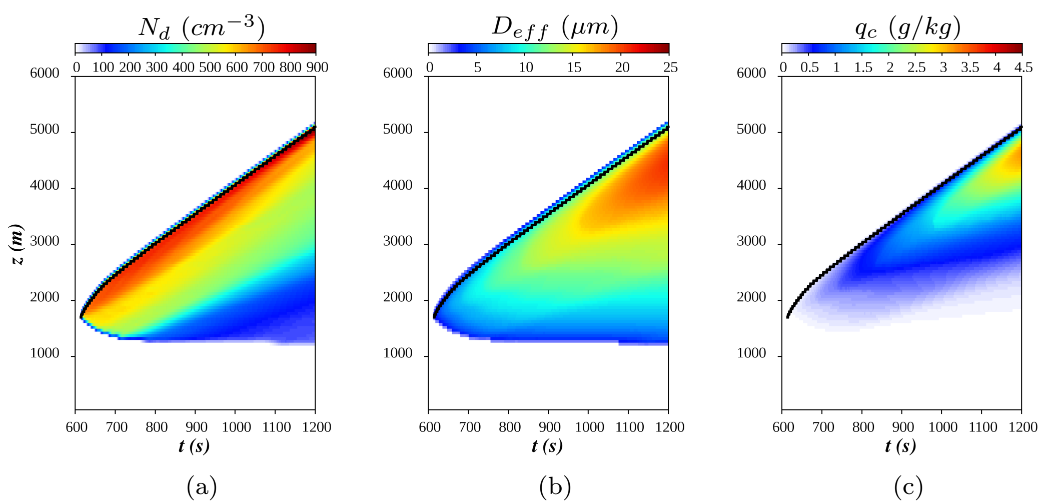

Figure 2. Evolution of N_d (cm^{-3}), D_{eff} (μm) and q_c (g/kg) in the simulation. The black lines represent cloud-top.

The Gamma phase spaces illustrated in Fig. 3 show the DSD evolution in the warm cloud that was simulated by the bin microphysics parameterization and the DSD evolution computed by Cecchini et al. (2017b) using measured DSDs. We tracked the evolution of the DSD at the top of the cloud for coherence with the AC09 sampling strategy. As already described, the simulation uses airplane and radiosonde data to reproduce nearly the same atmospheric state of those measurements. The large markers in Fig. 3b represent the averages for 200 m vertical intervals in the observation. Analogously, for time steps where the simulated cloud maintained the same maximum height, a mean cloud-top DSD was calculated. The simulation did not reach the highest levels sampled in the observations because it includes only the warm-phase processes. The projections of constant-D_{eff} surfaces ($D_{eff} = \frac{\mu+3}{\Lambda}$) are represented by red lines in the $\mu - \Lambda$ plane of Fig. 3a, from which it follows that the trajectory evolves from smaller to larger sizes, as expected. On the other hand, the progressive broadening of the DSDs is evidenced by the decrease in Λ and μ in both cases, while the number concentration increase manifests as larger values of N_0.

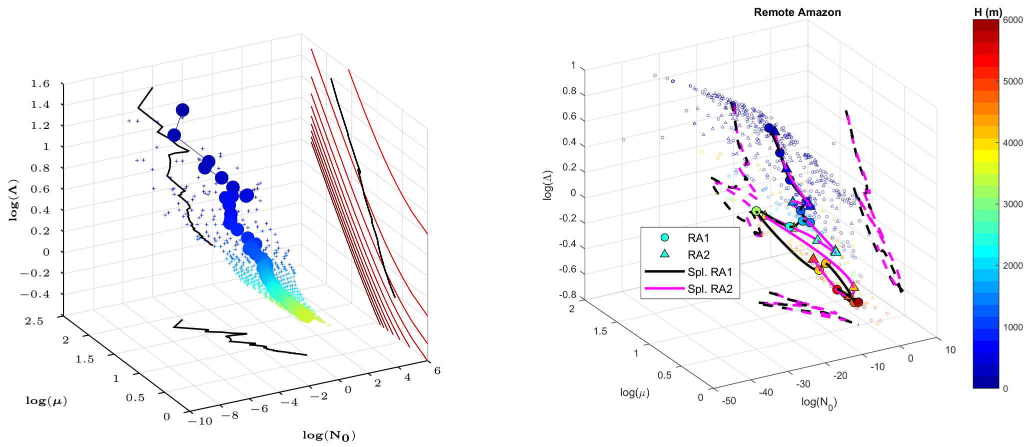

(a) (b)

Figure 3. Gamma phase space representation of cloud-top DSDs for different cloud widths: (a) bin microphysics simulation and (b) observation (Fig. 6 of Cecchini et al. (2017b)). Small markers represent 1 Hz data, while larger ones are averages for every model level in the simulation and for 200 m vertical intervals in the observation. The color scale represents the height above the cloud base in meters. Projections on axis planes are represented by black continuous lines, in the simulation, and dashed lines, in the observation. The red lines in (a) are the projections of the surfaces with constant D_{eff}, increasing from top to bottom.

At this point, it would be convenient to discuss more about how the DSD broadening manifests in terms of the Gamma parameters. The DSD width is conventionally associated to μ through the relative dispersion (ϵ) concept ($\epsilon = \frac{\sigma}{D_m} = \frac{1}{\sqrt{\mu+1}}$, where σ is the standard deviation and D_m is the mean diameter of the DSD). However, from the analyses of the gamma DSD properties – taking the first derivative of Eq. 1 –, we can see that the relation μ/Λ determines the location of the maximum concentration as well as its value, and the distance between the increasing and decreasing branches of the function. It means that decreasing μ, actually decreases those magnitudes. The interpretation depends on the definition of "broadening". While decreasing μ causes a relative broadening (expressed by the increase of ϵ), for an absolute broadening of the DSD, the decrease in μ must go along with a decrease in Λ.

It is interesting to note that, for increasing the effective diameter, there is no need for larger drops, a bigger quantity of the largest ones that already exist is sufficient. It should be also considered that the effective diameter is the ratio between two DSD moments of consecutive order (the second and third moments), the higher one being in the numerator. The higher the order of the moment, the more weight for larger droplets. Hence, if we increase the same amount of droplets for every bin, higher order moments will increase faster than smaller ones. Therefore, the effective diameter can increase even if every bin number concentration increases homogeneously.

The differences in absolute values between the graphics from Fig. 3 are determined by many factors. First, when dealing with the modeled cloud, the boundaries can be quantitatively defined; thus, there is more control over the path that follows the top of the cloud, as well as the position of the cloud base. Consequently, the initial portion of the graphic that represents the simulation includes information about the very beginning of the cloud, when the first droplets are activated and occupy only one or two bins of the DSD (leading to larger values of μ), while in the graphic that corresponds to the observation, the first DSDs plotted (lower heights above cloud base) correspond to a more developed stage of the cloud. This is why the simulated trajectory looks like an expanded version of the warm portion of the observed one. However, the qualitative similarity between the simulated and observed trajectories is quite remarkable, which ensures the bin microphysics simulation as a benchmark to study cloud processes and evaluate bulk parameterizations.

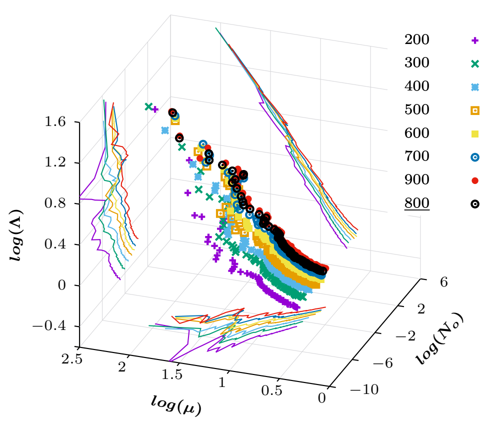

Figure 4. Illustration of the sensitivity of cloud-top DSDs to the initial aerosol number concentration in the Gamma phase space. The markers represent the average DSDs for each model level. Projections on axis planes are represented by continuous lines.

The description of the environmental conditions modulates the simulated DSD evolution and is also responsible for similarities and differences between the observed and simulated warm cloud evolution. For example, Fig. 4 shows that changes in the initial aerosol concentration can modify the position and shape of the simulated Gamma phase space trajectory by increasing the values of Λ and N_0 as an expression of more numerous droplets and narrower DSDs. The N_0 modification agrees with the well established dependence of the droplet number concentration on the number of aerosols. Also, note that the curves in the $\Lambda - \mu$ plane can be approximated by straight lines with different angular coefficients. The higher the coefficient is (in absolute terms) the faster the droplet growth will be, given the constant-D_{eff} surfaces described in Fig. 3. Because the cleanest case is associated to the highest coefficient, it evidences the fastest growth rate. Therefore, aerosols affect not only droplet number concentrations but also their growth rates throughout the whole warm phase – which is already studied in the literature and is usually justified by the water vapor competition.

3.2 Influence of the parameterization approach

In the previous section, we discussed how the evolution of the DSD, simulated by a bin microphysics scheme, can be modified by different atmospheric conditions, and it was exemplified through the sensitivity to the aerosol number concentration. However, in bulk schemes, there is an additional source of uncertainties due to the particularity of using a pre-defined DSD function, whose flexibility depends on the number of moments being predicted. The correct description of the DSD is important because it controls several physical processes, such as droplet growth, evaporation and sedimentation. Therefore, different Gamma parameters cause different bulk properties of the clouds, with consequences in the precipitation temporal and spatial distributions.

A common method in bulk parameterizations that uses gamma distributions for cloud droplets consists of fixing the μ parameter. Because Λ and N_0 depend on μ, they also become limited. Figure 5 illustrates the simulation obtained from a bin microphysics parameterization, as described above, compared to the one from a bulk single-moment parameterization (Thompson et al., 2008) (hereafter "thompson08"). The Gamma phase space trajectories for both simulations are very different, much more than the trajectories obtained from simulations with changes in the physical parameters of the bin scheme (N_a), as was shown in the previous section. The thompson08 parameterization defines μ as a fixed parameter that is inversely proportional to the cloud droplet concentration, with a value between 2 and 15 (Eq. 3). However, that relation does not provide the DSD evolution during the cloud life cycle, as described by observations or simulated with the bin scheme (Sect 3.1). It occupies a completely different portion of the Gamma phase space, and its evolution direction is somehow opposite to that from the bin scheme. This result occurs because, keeping μ constant, the initially narrow DSD has to be represented by higher values of N_0.

To avoid performing a comparison that involves accumulated errors, thus inducing larger differences in the DSD evolution, we also consider a hypothetical situation where, at every moment, the bulk scheme has the same values as the mixing ratio (and the concentration, when using a two-moment scheme) predicted by the bin scheme. This is also illustrated in Fig. 5 for the thompson08 and morrison09 (Morrison et al., 2009) parameterizations ("bin-based" label in the legend). This figure shows that, even if they were based on the correct values of the DSD moment(s), its DSD representation will be incorrect due to inefficiencies in the definition of the Gamma parameters' dependence on those moments.

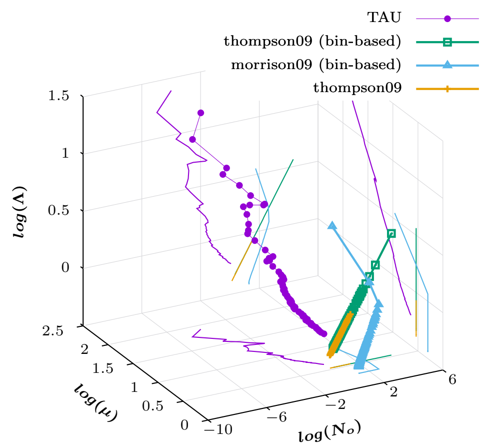

Figure 5. Phase space representation of the cloud-top layer when using TAU and thompson08 parameterizations, and the thompson08 and morrison09 approaches based on the moment(s) predicted by the TAU (bin-based). Projections on axis planes are represented by continuous lines.

As explained in Sect. 2.4, for fitting a gamma distribution to the DSDs of the bin scheme, we use the 0^{th}, 2^{nd} and 3^{rd} moments. Thus, the value of μ here should be a function of these variables, as defined by Eq. 8. However, Fig. 6a illustrates that μ is mostly determined by the magnitude of the 3^{rd} moment. Then, we can approximate μ at the cloud top as being inversely proportional to q_c, which is conveniently the variable predicted by one-moment bulk schemes (Eq. 10). Note that Eq. 10 was defined by adding a q_c-dependent term to the expression for μ originally employed by the thompson08 scheme (Eq. 3).

$$\mu(q_c) = \frac{1}{q_c} + \frac{1000}{N_d} + 2 \tag{10}$$

Defining μ according to Eq. 10, without any modification to the way in which Λ and N_0 are calculated, it is possible to reproduce the main characteristics of the bin simulation path in the Gamma phase space. This is illustrated in Fig. 6b, where we have used Eqs. 5, 6 and 10 with the moments produced by the bin simulation to generate a bin-like path in the Gamma phase space ("MOD" label in the figure).

The μ-modified path in Fig. 6b, similar to the ones corresponding to the original approaches used in the thompson08 and morrison09 schemes in Fig. 5, was obtained from the moments predicted by the bin to avoid other types of errors that could exist on those parameterizations. To analyze the direct effect of the proposed modification in one-moment bulk parameterizations, we used the thompson08 scheme. N_d in Eq. 10 was defined as 700 cm^{-3} for the thompson08 tests, as in Fig. 6a, but it must be variable if implemented in a two-moment scheme. Although the bin scheme can deal with extremely narrow DSDs, characterized by high values of μ that appear at the beginning of cloud development, allowing such a variation in μ does not perform well in the thompson08 scheme. Initially, small amounts of q_c would generate relatively high values of μ; the evolution

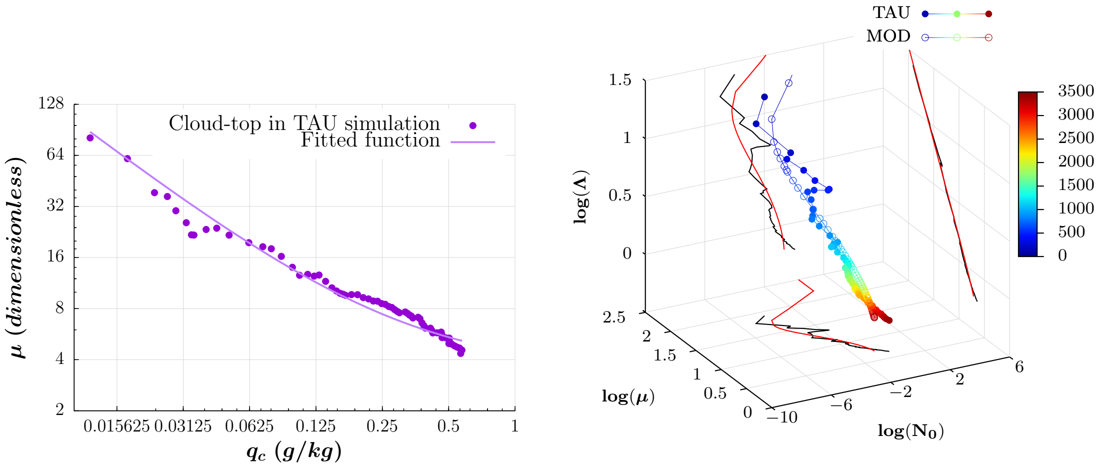

(a) (b)

Figure 6. (a) Relation between μ and q_c as obtained from the bin simulation cloud-top DSDs, (b) Gamma phase space representation of the cloud-top DSDs using a bin parameterization (TAU) and a modified approach for application in bulk schemes (MOD) based on the moment(s) predicted by the bin parameterization. The color scale corresponds to the height in meters. Projections on axis planes are represented by continuous lines, black ones for TAU and red ones for MOD.

of the DSD would then remain very limited, and no clouds would develop. The determination of the specific feature(s) of this scheme that could be responsible for such behavior is beyond the scope of this paper. For now, taking into account that the thompson08 scheme considers a variation of μ between 2 for continental and 15 for maritime, according to the general dispersion characteristics from Martin et al. (1994) and the results of Cecchini et al. (2017b), we defined a threshold of 20 as an upper bound on μ for the tests implemented here.

The effects of that modification on some bulk variables at the simulated cloud top are illustrated in Fig. 7. The droplet effective diameter and the rain-drop mixing ratio corresponding to the TAU simulation were inferred from the moments of the DSD that it predicts explicitly. In the case of the bulk scheme (original and modified), the droplet effective diameter was obtained from its Gamma parameters, and the values of the rain-drop mixing ratio are the ones predicted explicitly by the scheme.

The new approach improves the bulk simulation through a reduction in the droplet effective diameter (Fig. 7a). This modification of the DSD has a positive effect on the temporal distribution of the rain-drop mixing ratio (Fig. 7b) by determining its rates of conversion from cloud droplets. The cloud water mixing ratio remains unaltered because, at this stage, the amount that is being converted to rain is too small to cause an important sink effect and because, in this parameterization, the rates of cloud water production are not affected by the DSD shape.

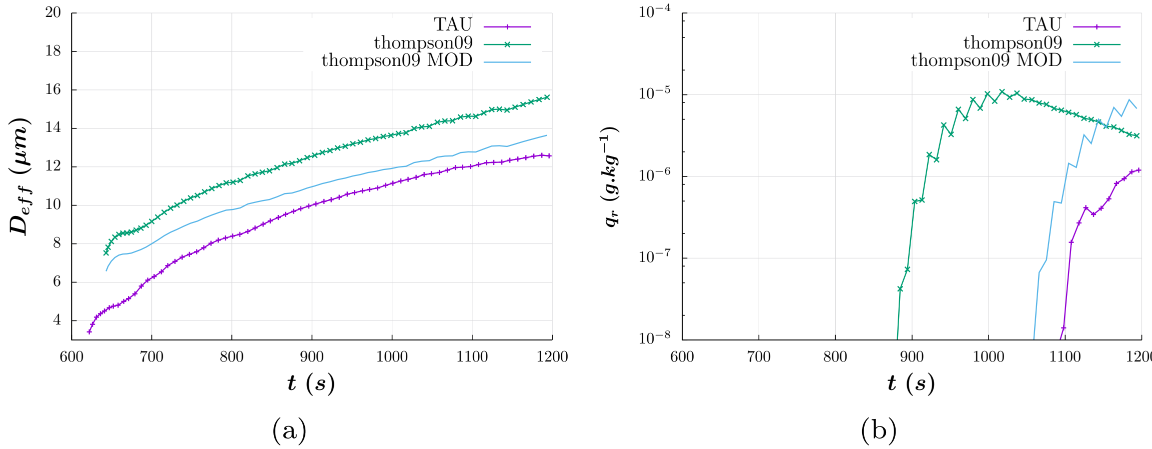

Figure 7. Comparison of the evolution of cloud-top properties in bin and bulk simulations before and after modifying μ: (a) droplet effective diameter and (b) rain-drop mixing ratio

Toward the interior of the cloud, the cloud-to-rain conversion rates should be larger. Then, a proportional decrease in droplet growth rates would cause an increase in the cloud water content with respect to the original scheme, and an adjustment of the rate of condensation may be necessary. Nevertheless, note that as q_c increases, μ tends to a fixed value, determined by the last two terms in Eq. 10. Hence, the expression for μ that we are proposing mainly modifies the beginning of the cloud development at each level, i.e. cloud top. Improving the representation of the DSD at the cloud top would strongly impact the evolution of the cloud given that it introduces a correction in the start point for each layer during cloud growth. Such a correction in the initial DSD modulates the rates of microphysical process onward, determining the structure of the cloud. If the simulation continues, both warm phase processes and the ice processes would be affected, which depend on the DSD when dealing with phase transitions and mechanical interactions between ice and liquid water. To explore these aspects, we tested the q_c-dependent expression for μ in a 3D real-case simulation at cloud resolving scale, which is presented in the next section.

3.3 Effects on a cloud resolving model simulation

In order to analyze the effects of the proposed expression for μ in the context of a more realistic, complex simulation, we use the WRF model with the parameterization of morrison09 and the configuration described in section 2.2. Figure 8 shows the reflectivity obtained from the 2km-altitude model output corresponding to 2200UTC and the 2km CAPPI from the São Roque radar at 1900 and 1930 UTC. It can be observed that the model represented a fairly symetric, continuous squall line, that is located perpendicular to the coast line and displaces toward the Northeast direction, parallel to the coastline. Its orientation and movement direction agrees well with the observation, however, the radar shows a more dispersed system, with a larger amount of stratiform areas.

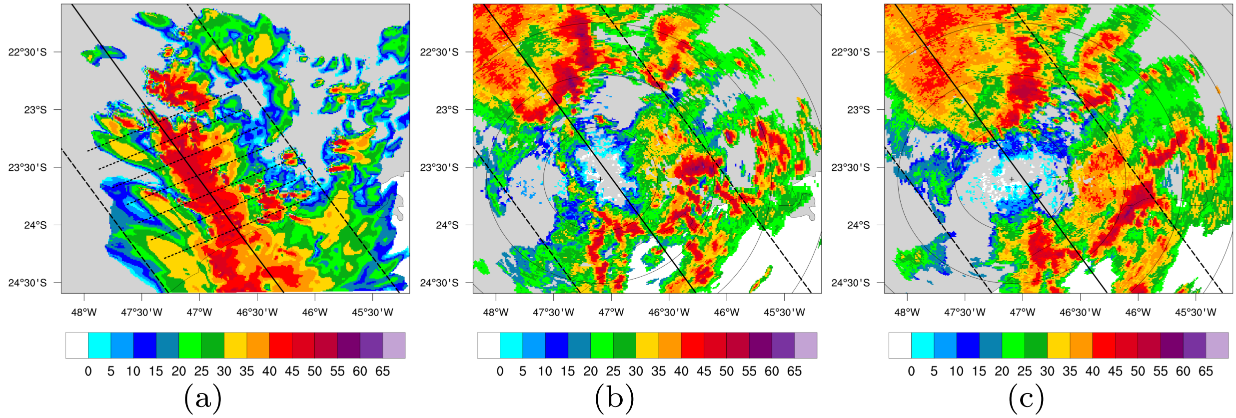

Figure 8. Reflectivity (dBZ) at 2km ASL from (a) the model output at 2200 UTC and (b),(c) São Roque radar scans at 1900 UTC and 1930 UTC respectively.

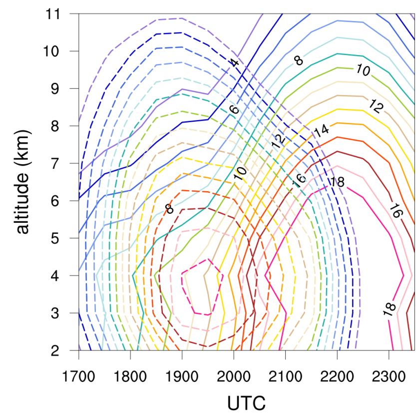

Figure 9. Evolution of the mean reflectivity in the region limited by long dashed lines in Fig. 8. The long dashed contours correspond to the radar data, the continuous contours represent the control simulation, and the short dashed contours represent the modified shape-parameter simulation.

To have an objective measure of the time shift between the modeled and observed fields, we calculated the averages of the reflectivity from both the model and the radar inside the area limited by the long dashed lines in Fig. 8. Figure 9 shows the evolution and vertical structure of these averages. It can be observed that the model has a delay of about 2.5 hours, considering the location of the maximum reflectivity, or 3 hours, considering the maximum height of the tops. While in the model the maximum reflectivity coincides in time with the maximum top-height, in the radar they occur in different moments. The behavior found in the radar data is consistent with the evolution of the system from convective to stratiform. Whereas there is not such a transition in the model output, instead, stratiform and convective areas coexist in time, without reaching a purely stratiform stage. We can also observe an overestimation of the mean reflectivity obtained from the model output, comparing to the radar, which is also a consequence of the different ratio of stratiform to convective areas. In the model, convective areas predominate over stratiform, and the opposite occur in the observation.

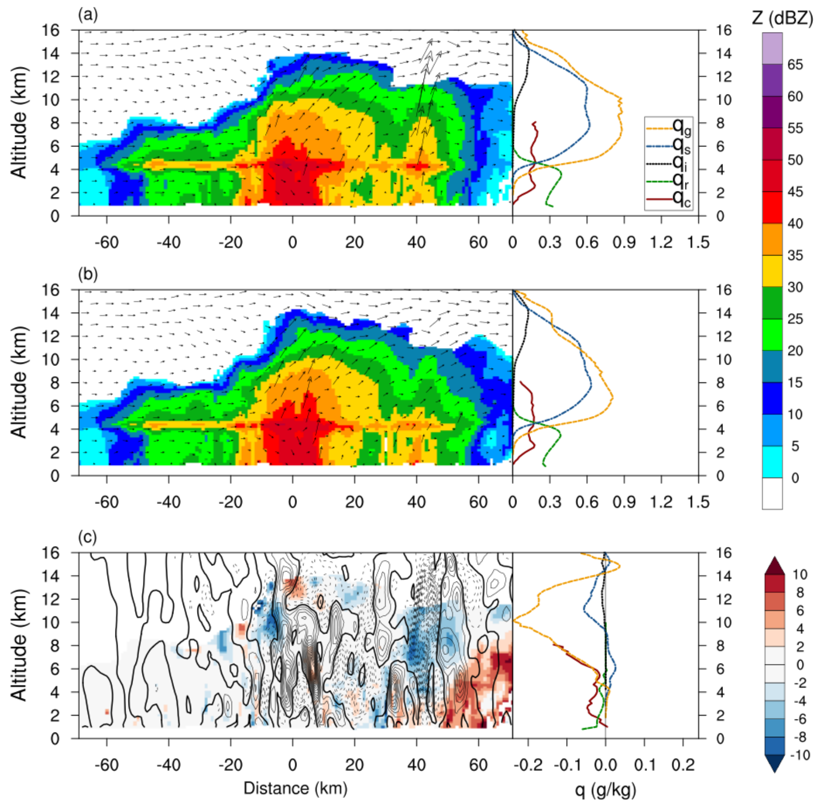

Figure 10. Average of the cross sections illustrated by the short dashed lines in Fig. 1 for: (a) the control simulation, (b) the simulation including the modified parameter, and (c) the difference field (modified-control). The left panels in (a) and (b) illustrate the reflectivity (dDZ) by color scale, and the wind speed (km/h) and direction by vectors. The left panel in (c) illustrates the difference (modified-control) of the reflectivity and the difference of the vertical component of the wind from the two simulations by color scale and contours, respectively. Continuous contours are for positive differences, and dashed contours are for negative differences. The right panels in (a) and (b) contain the profiles of hydrometeor mixing ratio (g/kg) averaged along the cross sections. The right panel in (c) contains the difference of those profiles from the two simulations.

The black continuous line in Fig. 8 indicates the center of the squall line in the simulation. Vertical cross sections oriented perpendicular to the squall line (short dashed lines in Fig. 8a) were used to analyze the vertical structure of the system and the effect of the microphysics modification on it. Figure 10 shows the average of the reflectivity in the cross sections and the averages of the hydrometeors profiles through them, for both the control and μ-modified simulations. In Fig. 10a and 10b, the vectors represent an average of the projections of the wind on each cross sections. To better visualize the behavior of the updraft velocity, we artificially decreased the horizontal component of the wind projections by a factor of 4 in the figures. Figure 10c shows the average of the difference between the two simulations for the reflectivity and the vertical velocity. Positive values, represented by red shadows and continuous contours stand for increments in the corresponding magnitude in the μ-modified simulation, compared to the control simulation.

It can be observed in Fig. 10 that the modified microphysics causes a decrease of the reflectivity at the edges of the storm, as expected, because the modification for μ acts at low cloud water mixing ratio. Interestly, the largest modifications are found at upper levels, where ice and mixing phase processes take place. There are regions where we can see the opposite effect, i.e. an increase of the reflectivity, mainly at the center and eastern boundary of the storm. However, the balance through the cross sections points toward a decrease of the reflectivity, which is evidenced in the behavior of the averaged hidrometeor profiles (right panels in Fig. 10). It can be seen that the overall effect is a decrease of the mixing ratio of cloud droplets, rain, ice crystals, snow and a remarkable diminution of graupel.

In the morrison09 parameterization, the processes that modify the cloud droplet specie are: activation, autoconversion, freezing, accretion by rain, ice, snow and graupel, and sedimentation. Considering the conversion rate equations used by the microphysics scheme, only freezing and sedimentation are directly affected by the value of μ. They both decrease as μ increases. Then, one would expect to have an increase of the cloud water, because of the weakening of the sinks in the cloud water tendency equation. However, since all the source and sink processes are a function of q_c they would be also favored forward in time. Taking into account the modification of the vertical velocity through changes in the latent heat release/absorption, we obtain a much more complex picture. Hence the importance of analyzing the responses to the modification in the microphysics in the context of a cloud resolving model.

In Fig. 10 it can be observed that the vertical velocity field exhibits a large variation from one simulation to another. Compared to the control simulation, the updrafts in the μ-modified run are enhanced at the center of the storm and diminished at the periphery, which is significantly correlated with the changes in the reflectivity. Note that, in the control simulation, there is a strong updraft core 40 km ahead of the main reflectivity nucleus that becomes remarkably attenuated.

The behavior of the averaged cloud water mixing ratio in the selected cross sections is illustrated in Fig. 11. The -4°C threshold, where freezing starts in the parameterization, is illustrated by the black continuous line in Fig. 11a and 11b. Note that the local maximum of q_c in the μ-modified simulation tend to be located at levels higher than in the control simulation, as a result of a smaller sedimentation rate and a less intense freezing. As a consequence, less latent heat is released, inhibiting updraft invigoration. This is the case of the updraft core located 40 km downwind of the the storm. Once q_c is sufficiently high, μ tends to the same value in both simulations. In that case, such as in the center of the storm, the droplet freezing is accelerated, invigorating the updraft. In Fig. 11c, it can be observed a pattern of alternating positive and negative variations of q_c, which evidences changes in the position of the clouds, in accordance with the changes in the vertical velocity.

The conversion rates from cloud water to rain in morrison09 are a growing function of q_c. For that reason, q_r seems to be well correlated to q_c at warm temperatures (below roughly 4 km ASL) in Fig. 12. It can be seen that the amount of rain is reduced from the control to the μ-modified simulation, as a response to the lower content of cloud water at those levels. However, at negative temperatures, despite having more intense cloud water cores, there is no significant amount of rain droplets. The latter is explained by the presence of many sink processes for the rain, since at cold temperature the drops can be frozen and

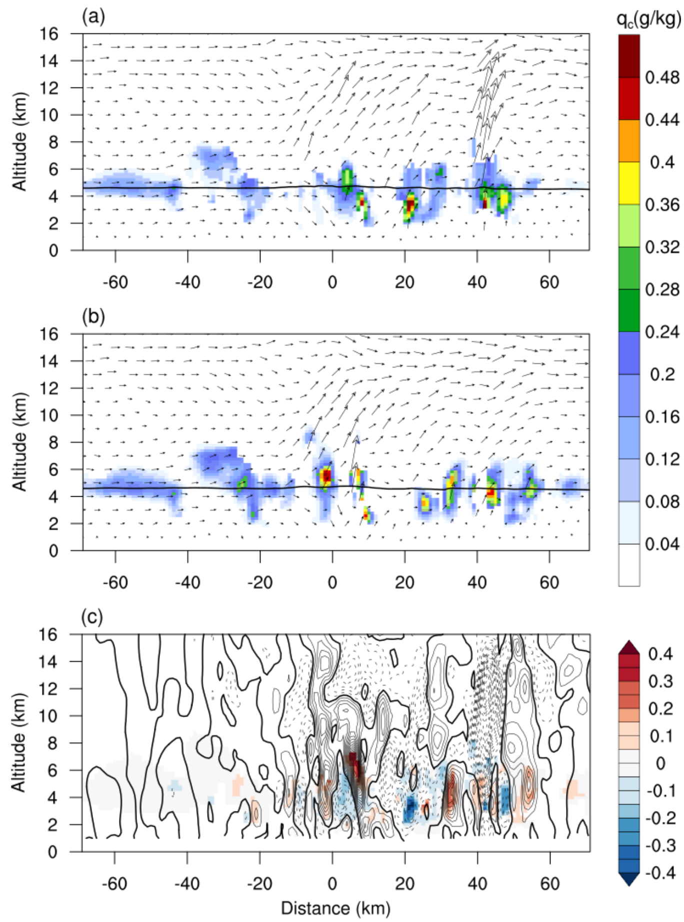

Figure 11. Similar to the left panels in 10 but for the cloud water mixing ratio. The black continuous line represents the -4°C isotherm

collected by snow and graupel, thereby consuming the mass of rain that could be created by autoconversion and collection of cloud droplets.

The largest content of ice crystals is found between 10 km and 16 km ASL in Fig. 13. It evidences a strong response to the intensity of the updraft. In the μ-modified simulation, the ice core located above the center of the storm became more intense, due to the increase of the updraft, while the maximum located right above the updraft 40 km ahead is remarkably decreased.

The same behavior is shown by the snow and the graupel mixing ratios in Fig. 14 and Fig. 15, respectively. However, the rate of increase of the snow at the center of the storm is larger than for the graupel, i.e., the snow responses faster than graupel. That difference comes from the thresholds the parameterization considers to allow graupel growth by collision-coalescence, in order to emulate the transition from snow to graupel in nature. For graupel to growth from collision-coalescence between ice crystals, snow and rain in the parameterization, the mixing rations of the latter two must be larger than 0.1 g/kg. This is particularly important at this stage because, as commented earlier in this section, the content of rain available above 4 km

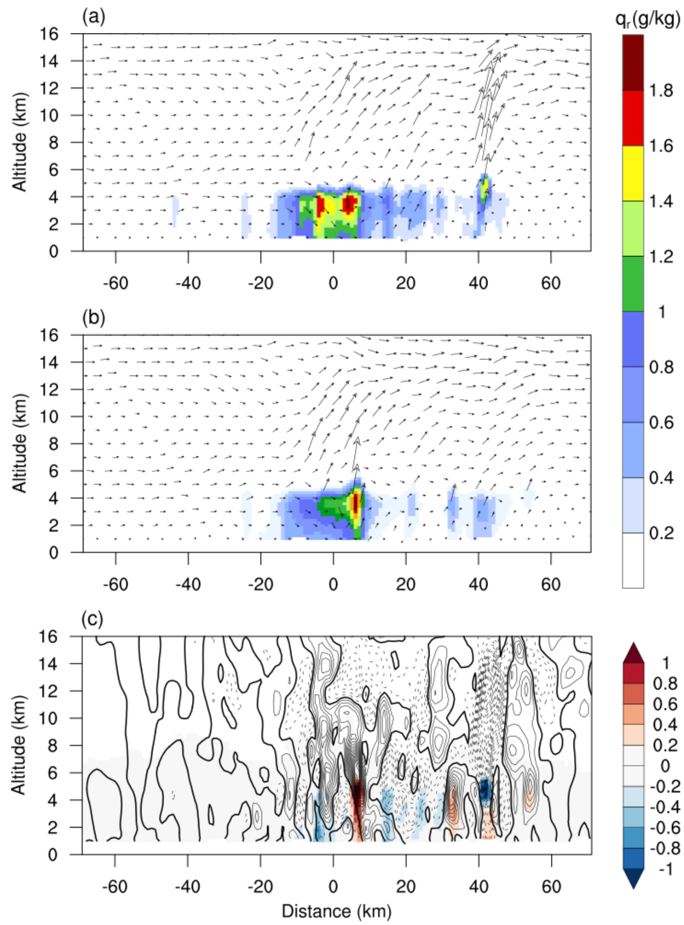

Figure 12. Similar to 11 but for the rain mixing ratio.

ASL is too low. An exception of that situation if found at about 6 km downwind of the storm, where the largest updraft in the μ-modified simulation is located. At this point, the amount of rain content reaches its maximum between 3-4 km ASL, and it can be observed that at 5 km ASL, q_r is approximately 0.4 g/kg. Coherently, the maximum increase of graupel is found in the same location, just next to the maximum increase of snow, which occurs at about 5 km downwind of the storm center.

Figure 16 illustrates the distribution of hidrometeors at the Northest cross section in both simulations. The mask was constructed by determining the hidrometeor with the largest mixing ratio at each point. Also, as the range of mass depends on the nature of each hidrometeor, a lower threshold was used for the mixing ratio of each specie: 0.3 g/kg for cloud droplets, 1.2 g/kg for rain, 0.3 g/kg for ice, 0.6 g/kg for snow and 3.5 g/kg for graupel. The thresholds were chosen in way that represent the contours where the largest differences between the simulations become evident. Those differences show the same behavior discussed above for the averaged fields of hidrometeors from the control to the μ-modified simulation.

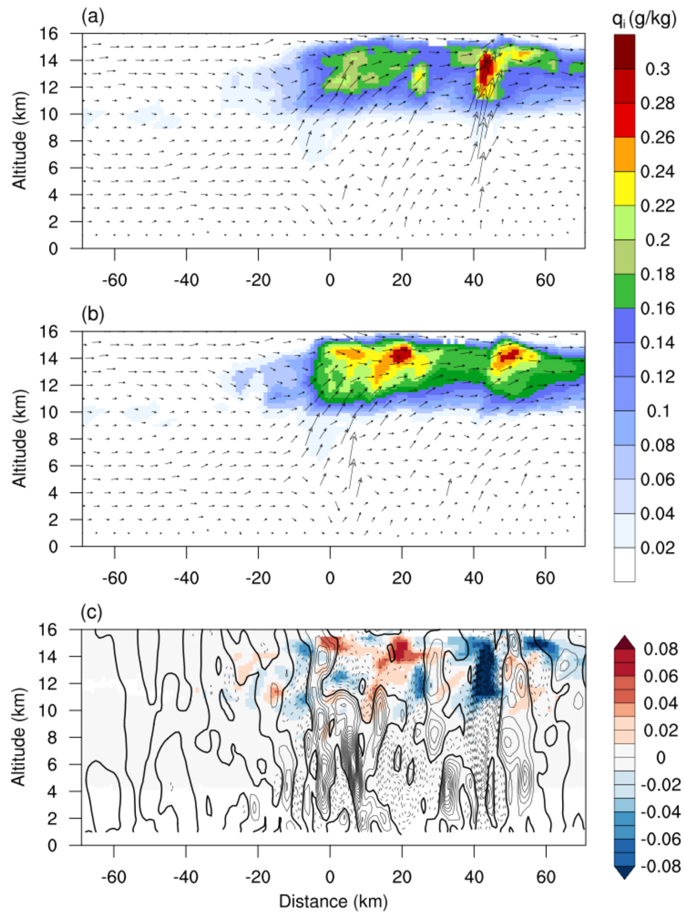

Figure 13. Similar to 11 but for the ice crystal mixing ratio.

For comparison, Fig. 17a shows the RHI from the dual polarization X-band radar located in Campinas, in the direction of the nucleus located at (-23.75;-47.25) in Fig. 8b, which has the largest VIL within the selected area (area between long dashed lines in Fig. 8c) and is close to the location of the model Northest cross section. It is not possible to use the 1930 UTC data from the X-band radar, because its signal was highly attenuated by rain at that time. Figure 17b illustrates the hidrometeor classification obtained from the radar data.

The structure of the cloud in the model outputs is qualitatively coherent with the radar observation. However, performing a quantitative comparison is difficult for several reasons. In the first place, assigning peers of analogous clouds in the observation and the simulation is non trivial, if not impossible, because at this scale, location error becomes more evident, as well as structural differences, such as erroneously merged or split cells. Also, even if there were a reasonable spatial correspondence between both fields, the similarities/dissimilarities between the members of one peer of cells observation-simulation can not be generalized a priori to all peers. Finally, the classification of hidrometeors from the radar data provides the hidrometeor type that is most probably to predominate in a point or an air parcel, but it does not determine quantitative information such

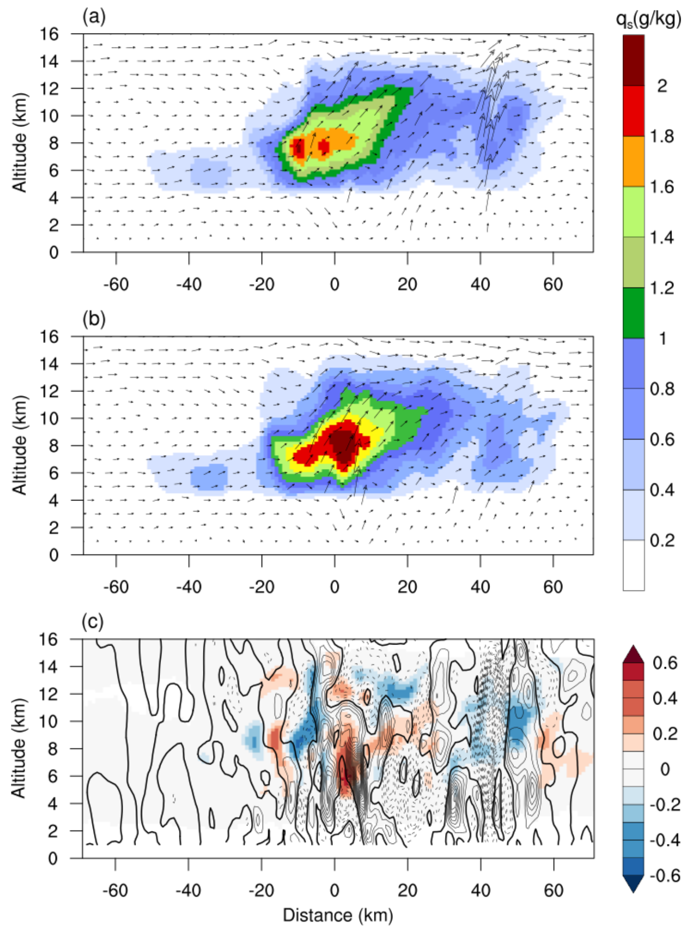

Figure 14. Similar to 11 but for the snow mixing ratio.

as mass or particle number. Besides, for the radar to detect the presence of an hidrometeor, there is a lower threshold for its mass/number that is much higher than the lower limit of the content of hidrometeors in the model. Therefore, in order to obtain an structure in the model that is coherent with the patterns the radar detects, we need to define empirical thresholds than can be adjusted as much as wanted to make the modeled pattern to resemble the observed one, thus limiting the reliability of the method.

Until now, we were able to determine the influence of the proposed closure formulation in a cloud resolving, real case simulation. We have proven that it has important microphysical and dynamical implications. Hence, the next step should be to investigate whether they improve the results, compared to the observation. For that purpose, we calculated the frequency distribution of the reflectivity at selected levels of the model output and radar CAPPIs. For the relative frequency calculations we used 70 bins of reflectivity between 0 dBZ and 70 dBZ and considered the total amount of points with $Z > 0$ dBZ at each

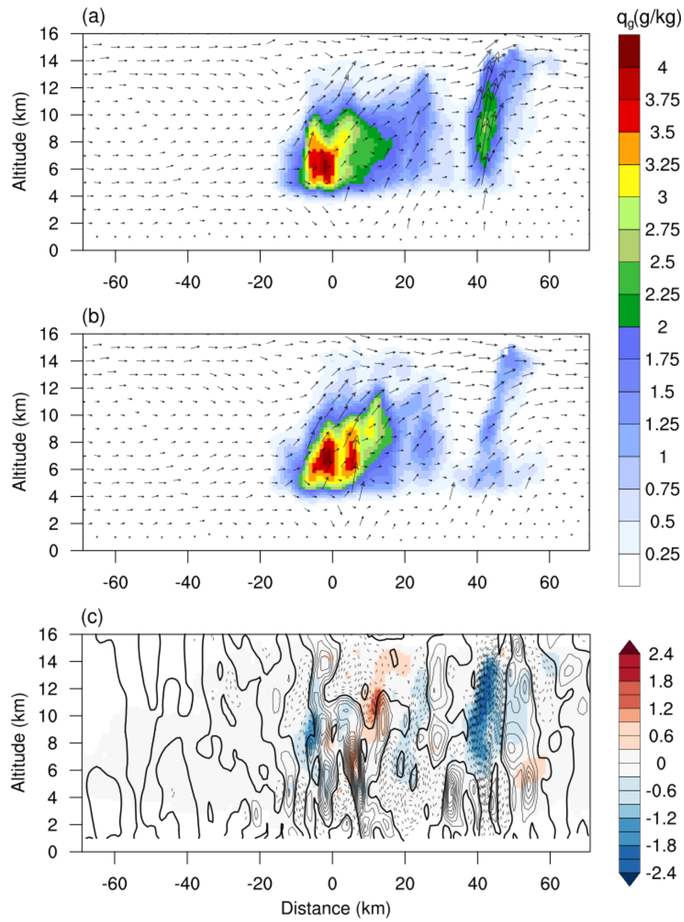

Figure 15. Similar to 11 but for the graupel mixing ratio.

level, i.e., for each height, the sum of the relative frequency over all the bins is 100. Figure 18 shows the contoured frequency by altitude diagram (CFAD) for the radar data and the control and μ-modified simulations.

One of the majors differences between the model and the radar, according to its CFADs, lies on the dispersion of the frequencies. Figure 18a shows that in the radar data, there is less variety of the reflectivity, compared to the model. Values of Z below 10 dBZ are very rare in all levels, while the reflectivity value where the upper threshold of 0.4 is located decreases with height, as well as the dispersion of the values. This characteristic causes the maximum of the relative frequency to be larger than in the model, specially at the upper levels, where the dispersion is minimum. Both model CFADs, Fig. 18b and 18c, shows a large dispersion of the reflecitivity; values of Z near 0 are relatively common at all levels, and the location of the upper threshold of 0.4 has a small variation with height. However, the location of the maximum frequency in the model CFAD has a notable variation with height, larger than the radar: the higher the height, the more frequent low values of Z are.

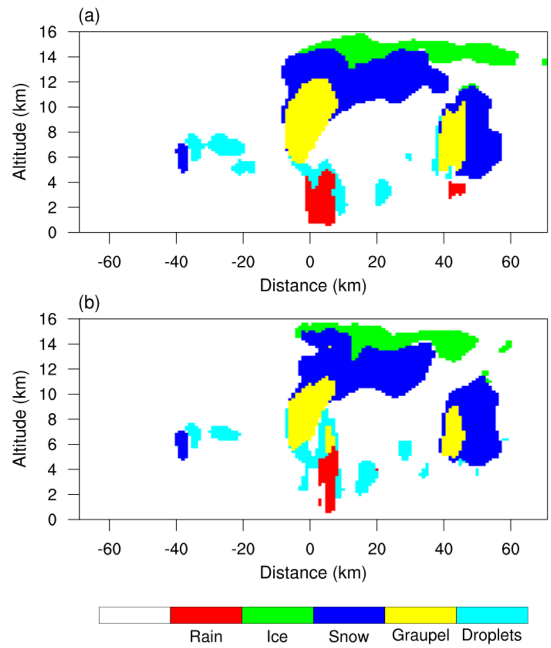

Figure 16. Hidrometeor classification mask for the Northest cross section in Fig. 8

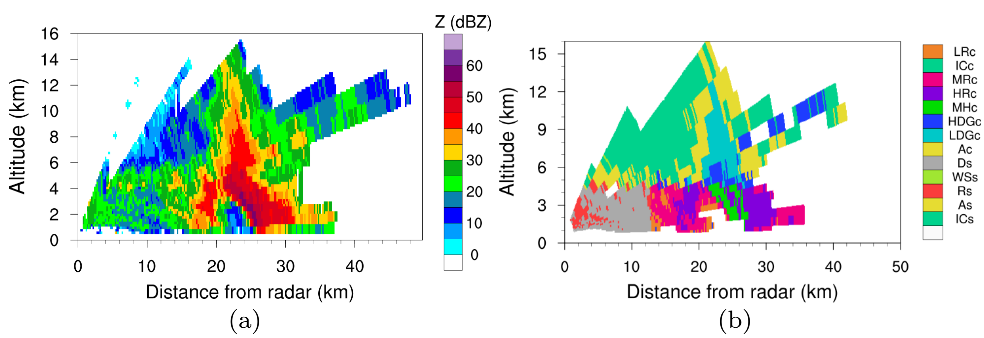

Figure 17. RHI from the Campinas radar in the direction of the nucleus located at (-23.45;-47.15) in Fig. 1b: (a) Reflectivity, (b) Hidrometeor classification

The small frequency of low reflectivity values in the radar may be related to a deficient measurement, note that those values appear near the location of the radar in Fig. 8b and becomes less frequent as the distance increases, suggesting a diminution of the capacity of the radar for detecting that kind of signal with distance. However, the larger frequency of high reflectivity values in the model is clearly the result of the excess of convection created by the model, such as the portion of the squall line closer to the position of the radar, which does not exist in the observation, and the lack of statriform areas, such as those detected by the radar at the Northwest portion of the domain. These features would give a larger weight to values of Z around 30 dBZ, therefore decreasing the relative frequency of the largest values of Z. Another misrepresented aspect in the model

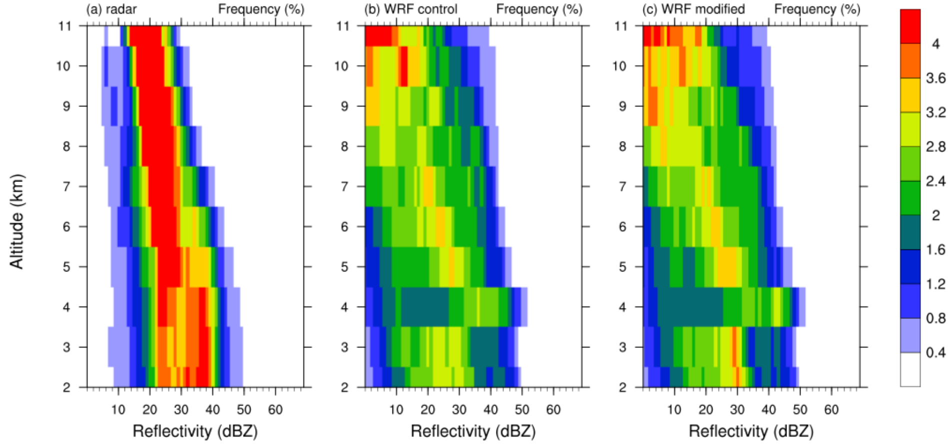

Figure 18. CFADs relative to the total amount of points in the area of interesest

is the intensity of the bright band which is remarkably overestimated, probably as a result of the excessive production of ice species.

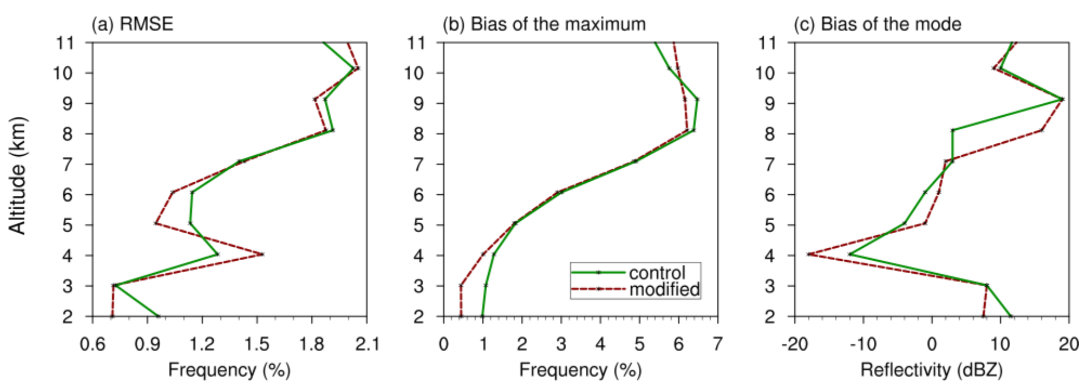

Figure 19. Comparison of the CFADs obtained from radar and model simulation (a) RMSE centered at the maximum frequency, (b) BIAS of the maximum frequency, (c) BIAS of the more frequent value of reflectivity

In Fig. 18, it can be seen that the maximum of the relative frequency exhibits larger values in the μ-modified simulation, accompanied by a less evident decrease in the frequency of the extreme values of Z. Figure 19 illustrates the behavior of some indexes that provide a quantitative comparison between radar and model CFADs. In order to avoid penalization due to the errors in location, we calculated the root mean square error (RMSE) based on the position of the maximum value of Z at each height. In other words, to calculate the point-by-point errors between the CFADs, we consider that the graphs are overlapped at the maximum Z at each height. Figure 19a shows that the RMSE corresponding to the μ-modified simulation is smaller than the RMSE of the control simulation at most of the levels, which also evidences in a smaller bias of the maximum frequency, as mentioned before. The bias of the position of the maximum, or the mode value (Fig. 19c), became closer to zero at levels below

8 km, except at 4 km, where the bright band is located. Above 7 km, despite the position of the maximum is not improved, it can be seen in Fig. 18 that an improvement is obtained through a tendency to increase the frequency of higher values of Z.

4 Concluding remarks

To validate the skills of the microphysics parameterizations, the cloud-top trajectory in the Gamma phase space corresponding to in situ measurements was taken as a reference. The bin scheme was able to reproduce the main features of the observed DSD evolution, representing the progressive broadening of the DSDs as an increase in N_0 and a decrease in Λ and μ in the Gamma phase space. The agreement between the observed and bin-simulated warm cloud evolution is determined by the description of environmental conditions, such as the aerosol content. The simulation added information about earlier stages of cloud development thanks to the possibility of defining an objective criterion for the cloud initiation time and the position of its boundaries. These results allowed us to consider the bin microphysics parameterization as a valuable benchmark, useful for analyzing the dependence of the system responses on several parameters that characterize the environmental conditions and for evaluating the suitability of bulk microphysics approaches.

The Gamma phase space representation of the cloud top is highly affected by the approach chosen for the microphysics parameterization. Whereas the bin scheme approximately resembles the observations, bulk approaches generate completely different signatures, mainly in terms of its evolution direction. In an attempt to correct those deficiencies, we proposed an adjustment to bulk parameterizations based on the calculation of the μ parameter according to the mixing ratio of cloud droplets. The new approach provides a bin-like path in the Gamma phase space that corrects the cloud-top representation in bulk schemes. When this modification is introduced in the scheme of Thompson et al. (2008), the droplet effective diameter is reduced, with favorable consequences in the amount of precipitation.

The new expression for the μ parameter was also tested in the WRF model, with a cloud resolving configuration, using the parameterization of Morrison et al. (2009). It was found to produce notable changes in the reflectivity obtained from the model output, due to modifications in the content of rain, snow and graupel, as well as in the structure of the convective system. Since the value of μ becomes higher at low cloud water mixing ratios, it influences primarily the parts of the cloud that are closer to its boundaries. Changes in the intensity of the latent heat release, related to a slower droplet freezing, significantly decrease the updraft velocity in a cell located 40 km downwind of the center of the storm. The CFAD analysis evidenced that the proposed expression for μ improves the distribution of the reflecitivity frequency in the model, when compared to the radar.

Acknowledgements. This research was funded by the SOS CHUVA FAPESP Project 2015/14497-0. The contributions of Micael A. Cecchini and Lianet H. Pardo were funded by FAPESP grants 2017/04654-6 and 2016/24562-6, respectively.

References

Berry, E. X. and Reinhardt, R. L.: An analysis of cloud drop growth by collection: Part I. Double distributions, Journal of the Atmospheric Sciences, 31, 1814–1824, 1974.

Cecchini, M. A., Machado, L. A. T., Andreae, M. O., Martin, S. T., Albrecht, R. I., Artaxo, P., Barbosa, H. M. J., Borrmann, S., Fütterer, D., Jurkat, T., Mahnke, C., Minikin, A., Molleker, S., Pöhlker, M. L., Pöschl, U., Rosenfeld, D., Voigt, C., Weinzierl, B., and Wendisch, M.: Sensitivities of Amazonian clouds to aerosols and updraft speed, Atmospheric Chemistry and Physics, 17, 10 037–10 050, 2017a.

Cecchini, M. A., Machado, L. A. T., Wendisch, M., Costa, A., Krämer, M., Andreae, M. O., Afchine, A., Albrecht, R. I., Artaxo, P., Borrmann, S., Fütterer, D., Klimach, T., Mahnke, C., Martin, S. T., Minikin, A., Molleker, S., Pardo, L. H., Pöhlker, C., Pöhlker, M. L., Pöschl, U., Rosenfeld, D., and Weinzierl, B.: Illustration of microphysical processes in Amazonian deep convective clouds in the gamma phase space: introduction and potential applications, Atmospheric Chemistry and Physics, 17, 14 727–14 746, 2017b.

Charney, J. G. and Phillips, N.: Numerical integration of the quasi-geostrophic equations for barotropic and simple baroclinic flows, Journal of Meteorology, 10, 71–99, 1953.

Enukashvily, I. M.: A numerical method for integrating the kinetic equation of coalescence and breakup of cloud droplets, Journal of the Atmospheric Sciences, 37, 2521–2534, 1980.

Feingold, G., Tzivion, S., and Levin, Z.: The evolution of raindrop spectra with altitude 1: Solution to the stochastic collection/breakup equation using the method of moments, Journal of the Atmospheric Sciences, 45, 3387–3399, 1988.

Ferrier, B. S.: A double-moment multiple-phase four-class bulk ice scheme. Part I: Description, Journal of the Atmospheric Sciences, 51, 249–280, 1994.

Gilmore, M. S., Straka, J. M., and Rasmussen, E. N.: Precipitation uncertainty due to variations in precipitation particle parameters within a simple microphysics scheme, Monthly Weather Review, 132, 2610–2627, 2004.

Grabowski, W. W.: Toward Cloud Resolving Modeling of Large-Scale Tropical Circulations: A Simple Cloud Microphysics Parameterization, Journal of the Atmospheric Sciences, 55, 3283–3298, 1998.

Gunthe, S. S., King, S. M., Rose, D., Chen, Q., Roldin, P., Farmer, D. K., Jimenez, J. L., Artaxo, P., Andreae, M. O., Martin, S. T., and Pöschl, U.: Cloud condensation nuclei in pristine tropical rainforest air of Amazonia: size-resolved measurements and modeling of atmospheric aerosol composition and CCN activity, Atmospheric Chemistry and Physics, 9, 7551–7575, 2009.

Igel, A. L. and van den Heever, S. C.: The role of the gamma function shape parameter in determining differences between condensation rates in bin and bulk microphysics schemes, Atmospheric Chemistry and Physics, 17, 4599–4609, 2017.

Khain, A., Pokrovsky, A., Pinsky, M., Seifert, A., and Phillips, V.: Simulation of effects of atmospheric aerosols on deep turbulent convective clouds using a spectral microphysics mixed-phase cumulus cloud model. Part I: Model description and possible applications, Journal of the Atmospheric Sciences, 61, 2963–2982, 2004.

Khain, A., Lynn, B., and Dudhia, J.: Aerosol effects on intensity of landfalling hurricanes as seen from simulations with the WRF model with spectral bin microphysics, Journal of the Atmospheric Sciences, 67, 365–384, 2010.

Khain, A. P., Beheng, K. D., Heymsfield, A., Korolev, A., Krichak, S. O., Levin, Z., Pinsky, M., Phillips, V., Prabhakaran, T., Teller, A., van den Heever, S. C., and Yano, J.-I.: Representation of microphysical processes in cloud-resolving models: Spectral (bin) microphysics versus bulk parameterization, Reviews of Geophysics, 53, 247–322, 2015.

Lance, S., Brock, C., Rogers, D., and Gordon, J. A.: Water droplet calibration of the Cloud Droplet Probe (CDP) and in-flight performance in liquid, ice and mixed-phase clouds during ARCPAC, Atmospheric Measurement Techniques, 3, 1683–1706, 2010.

Leonard, B., MacVean, M., and Lock, A.: Positivity-preserving numerical schemes for multidimensional advection, bracknell, England: NASA STI/Recon Technical Report N 02/1993; 93:27091, 1993.

Lim, K.-S. S. and Hong, S.-Y.: Development of an effective double-moment cloud microphysics scheme with prognostic cloud condensation nuclei (CCN) for weather and climate models, Monthly Weather Review, 138, 1587–1612, 2010.

Lin, Y.-L., Farley, R. D., and Orville, H. D.: Bulk parameterization of the snow field in a cloud model, Journal of Climate and Applied Meteorology, 22, 1065–1092, 1983.

Loftus, A., Cotton, W., and Carrió, G.: A triple-moment hail bulk microphysics scheme. Part I: Description and initial evaluation, Atmospheric research, 149, 35–57, 2014.

Lorenz, E. N.: Energy and numerical weather prediction, Tellus, 12, 364–373, 1960.

Machado, L. A. T., Dias, M. A. F. S., Morales, C., Fisch, G., Vila, D., Albrecht, R., Goodman, S. J., Calheiros, A. J. P., Biscaro, T., Kummerow, C., Cohen, J., Fitzjarrald, D., Nascimento, E. L., Sakamoto, M. S., Cunningham, C., Chaboureau, J.-P., Petersen, W. A., Adams, D. K., Baldini, L., Angelis, C. F., Sapucci, L. F., Salio, P., Barbosa, H. M. J., Landulfo, E., Souza, R. A. F., Blakeslee, R. J., Bailey, J., Freitas, S., Lima, W. F. A., and Tokay, A.: The Chuva Project: How Does Convection Vary across Brazil?, Bulletin of the American Meteorological Society, 95, 1365–1380, 2014.

Mansell, E. R., Ziegler, C. L., and Bruning, E. C.: Simulated electrification of a small thunderstorm with two-moment bulk microphysics, Journal of the Atmospheric Sciences, 67, 171–194, 2010.

Martin, G., Johnson, D., and Spice, A.: The measurement and parameterization of effective radius of droplets in warm stratocumulus clouds, Journal of the Atmospheric Sciences, 51, 1823–1842, 1994.

Martin, S. T., Andreae, M. O., Artaxo, P., Baumgardner, D., Chen, Q., Goldstein, A. H., Guenther, A., Heald, C. L., Mayol-Bracero, O. L., McMurry, P. H., Pauliquevis, T., Pöschl, U., Prather, K. A., Roberts, G. C., Saleska, S. R., Dias, M. A. S., Spracklen, D. V., Swietlicki, E., and Trebs, I.: Sources and properties of Amazonian aerosol particles, Reviews of Geophysics, 48, 2010.

Milbrandt, J. and Yau, M.: A multimoment bulk microphysics parameterization. Part I: Analysis of the role of the spectral shape parameter, Journal of the atmospheric sciences, 62, 3051–3064, 2005a.

Milbrandt, J. and Yau, M.: A multimoment bulk microphysics parameterization. Part II: A proposed three-moment closure and scheme description, Journal of the atmospheric sciences, 62, 3065–3081, 2005b.

Miles, N. L., Verlinde, J., and Clothiaux, E. E.: Cloud droplet size distributions in low-level stratiform clouds, Journal of the atmospheric sciences, 57, 295–311, 2000.

Molleker, S., Borrmann, S., Schlager, H., Luo, B., Frey, W., Klingebiel, M., Weigel, R., Ebert, M., Mitev, V., Matthey, R., Woiwode, W., Oelhaf, H., Dörnbrack, A., Stratmann, G., Grooß, J.-U., Günther, G., Vogel, B., Müller, R., Krämer, M., Meyer, J., and F., C.: Microphysical properties of synoptic-scale polar stratospheric clouds: in situ measurements of unexpectedly large HNO 3-containing particles in the Arctic vortex, Atmospheric chemistry and physics, 14, 10 785–10 801, 2014.

Morrison, H. and Grabowski, W. W.: Comparison of Bulk and Bin Warm-Rain Microphysics Models Using a Kinematic Framework, Journal of the Atmospheric Sciences, 64, 2839–2861, 2007.

Morrison, H., Thompson, G., and Tatarskii, V.: Impact of Cloud Microphysics on the Development of Trailing Stratiform Precipitation in a Simulated Squall Line: Comparison of One- and Two-Moment Schemes, Monthly Weather Review, 137, 991–1007, 2009.

Pöhlker, M. L., Pöhlker, C., Ditas, F., Klimach, T., Hrabe de Angelis, I., Araújo, A., Brito, J., Carbone, S., Cheng, Y., Chi, X., Ditz, R., Gunthe, S. S., Kesselmeier, J., Könemann, T., Lavrič, J. V., Martin, S. T., Mikhailov, E., Moran-Zuloaga, D., Rose, D., Saturno, J., Su, H., Thalman, R., Walter, D., Wang, J., Wolff, S., Barbosa, H. M. J., Artaxo, P., Andreae, M. O., and Pöschl, U.: Long-term observations of cloud condensation nuclei in the Amazon rain forest – Part 1: Aerosol size distribution, hygroscopicity, and new model parametrizations for CCN prediction, Atmospheric Chemistry and Physics, 16, 15 709–15 740, 2016.

Reisin, T. G., Yin, Y., Levin, Z., and Tzivion, S.: Development of giant drops and high-reflectivity cores in Hawaiian clouds: Numerical simulations using a kinematic model with detailed microphysics, Atmospheric research, 45, 275–297, 1998.

Rotach, M. W. and Zardi, D.: On the boundary-layer structure over highly complex terrain: Key findings from MAP, Quarterly Journal of the Royal Meteorological Society, 133, 937–948, 2007.

Rotstayn, L. D. and Liu, Y.: Sensitivity of the First Indirect Aerosol Effect to an Increase of Cloud Droplet Spectral Dispersion with Droplet Number Concentration, Journal of Climate, 16, 3476–3481, 2003.

Shipway, B. and Hill, A.: Diagnosis of systematic differences between multiple parametrizations of warm rain microphysics using a kinematic framework, Quarterly Journal of the Royal Meteorological Society, 138, 2196–2211, 2012.

Stevens, B., Feingold, G., Cotton, W. R., and Walko, R. L.: Elements of the microphysical structure of numerically simulated nonprecipitating stratocumulus, Journal of the atmospheric sciences, 53, 980–1006, 1996.

Szyrmer, W., Laroche, S., and Zawadzki, I.: A Microphysical Bulk Formulation Based on Scaling Normalization of the Particle Size Distribution. Part I: Description, Journal of the Atmospheric Sciences, 62, 4206–4221, 2005.

Thompson, G. and Eidhammer, T.: A study of aerosol impacts on clouds and precipitation development in a large winter cyclone, Journal of the Atmospheric Sciences, 71, 3636–3658, 2014.

Thompson, G., Rasmussen, R. M., and Manning, K.: Explicit forecasts of winter precipitation using an improved bulk microphysics scheme. Part I: Description and sensitivity analysis, Monthly Weather Review, 132, 519–542, 2004.

Thompson, G., Field, P. R., Rasmussen, R. M., and Hall, W. D.: Explicit Forecasts of Winter Precipitation Using an Improved Bulk Microphysics Scheme. Part II: Implementation of a New Snow Parameterization, Monthly Weather Review, 136, 5095–5115, 2008.

Tzivion, S., Feingold, G., and Levin, Z.: An efficient numerical solution to the stochastic collection equation, Journal of the Atmospheric Sciences, 44, 3139–3149, 1987.

Tzivion, S., Feingold, G., and Levin, Z.: The evolution of raindrop spectra. Part II: Collisional collection/breakup and evaporation in a rainshaft, Journal of the Atmospheric Sciences, 46, 3312–3328, 1989.

Wendisch, M., Pöschl, U., Andreae, M. O., Machado, L. A. T., Albrecht, R., Schlager, H., Rosenfeld, D., Martin, S. T., Abdelmonem, A., Afchine, A., Araùjo, A. C., Artaxo, P., Aufmhoff, H., Barbosa, H. M. J., Borrmann, S., Braga, R., Buchholz, B., Cecchini, M. A., Costa, A., Curtius, J., Dollner, M., Dorf, M., Dreiling, V., Ebert, V., Ehrlich, A., Ewald, F., Fisch, G., Fix, A., Frank, F., Fütterer, D., Heckl, C., Heidelberg, F., Hüneke, T., Jäkel, E., Järvinen, E., Jurkat, T., Kanter, S., Kästner, U., Kenntner, M., Kesselmeier, J., Klimach, T., Knecht, M., Kohl, R., Kölling, T., Krämer, M., Krüger, M., Krisna, T. C., Lavric, J. V., Longo, K., Mahnke, C., Manzi, A. O., Mayer, B., Mertes, S., Minikin, A., Molleker, S., Münch, S., Nillius, B., Pfeilsticker, K., Pöhlker, C., Roiger, A., Rose, D., Rosenow, D., Sauer, D., Schnaiter, M., Schneider, J., Schulz, C., de Souza, R. A. F., Spanu, A., Stock, P., Vila, D., Voigt, C., Walser, A., Walter, D., Weigel, R., Weinzierl, B., Werner, F., Yamasoe, M. A., Ziereis, H., Zinner, T., and Zöger, M.: The ACRIDICON-CHUVA campaign: Studying tropical deep convective clouds and precipitation over Amazonia using the new German research aircraft HALO, Bulletin of the American Meteorological Society, 2016.

Yin, Y., Levin, Z., Reisin, T., and Tzivion, S.: Seeding convective clouds with hygroscopic flares: Numerical simulations using a cloud model with detailed microphysics, Journal of Applied Meteorology, 39, 1460–1472, 2000a.

Yin, Y., Levin, Z., Reisin, T. G., and Tzivion, S.: The effects of giant cloud condensation nuclei on the development of precipitation in convective clouds—A numerical study, Atmospheric research, 53, 91–116, 2000b.